Journal of Materials Chemistry C

ROYAL SOCIETY OF CHEMISTRY

PAPER

View Article Online
View Journal

Cite this: DOI: 10.1039/d6tc00748a

Trap-controlled operational stability in dibenzofuran-based hosts for blue TADF-OLEDs

Domantas Berenis,[a] Eigirdas Skuodis,[ab] Kristupas Bagdonas,[a] Goda Grybauskaitė,[a] Dovydas Banevičius,[a] Gediminas Kreiza,[a] Rita Butkutė,[ab] Juozas V. Gražulevičius[b] and Karolis Kazlauskas*[a]

Stability remains the principal bottleneck for blue TADF-OLEDs, and it is strongly affected by the host response to electrical stress. Here we report a structure–property study of four high-triplet-energy dibenzofuran–biphenyl (DBF–BPh) hosts for stable blue TADF devices. DBF linkage position (2 *vs.* 4) and *tert*-butyl substitution are exploited to tune solid-state charge dynamics within a chemically robust scaffold. All hosts exhibit high neat-film triplet energies (T_1 = 2.77–2.87 eV) suitable for blue/sky-blue exciton confinement, together with elevated multi-state bond dissociation energies (BDEs) that exceed the fragility range typical of anionic C–N linkages in common carbazole-type hosts. In doped blue TADF-OLEDs, the 4-linked DBF–BPh hosts deliver the best overall device performance, reaching EQE_{max} = 23.5% with low efficiency roll-off and device lifetime LT_{50} = 17.5 h at 1000 cd m^{-2} (275 h at 100 cd m^{-2}). In contrast, *tert*-butyl-substituted hosts exhibit 2–4× shorter LT_{50}, despite comparable energetics and BDE profiles. Bias-dependent impedance spectroscopy combined with equivalent-circuit analysis indicates a larger resistive relaxation component in the *tert*-butyl hosts, consistent with increased trap-limited conduction and carrier accumulation, which accelerate exciton–polaron loss under operation. These results implicate trapping as a major contributor to device degradation in this DBF host series, thereby establishing trap suppression as a practical target for improving the lifetime of blue TADF-OLEDs.

Received 9th March 2026,
Accepted 15th April 2026

DOI: 10.1039/d6tc00748a

rsc.li/materials-c

1. Introduction

Thermally activated delayed fluorescence (TADF) OLEDs enable the harvesting of electrically generated triplet excitons by reverse intersystem crossing (RISC), offering a pathway to near-unity internal quantum efficiency with purely organic emitters.[1–3] Over the past decade, this concept has translated into routinely high device-level efficiencies.[4,5] However, achieving a simultaneous combination of high external quantum efficiency (EQE) >20% and a long lifetime under high-brightness operation (~1000 cd m^{-2}) remains particularly challenging in the blue spectral region.[3,5–8]

The intrinsic challenge of blue TADF stability pertains to the high excited-state energies required for blue emission and the long-lived triplet population that accumulates under electrical excitation. High-energy species generated *via* exciton–exciton/polaron loss channels can initiate chemical transformations and irreversible degradation, with rates that increase strongly under practical luminance and current densities.[3,9–11] In the blue regime, these annihilation events are particularly damaging because they can create excitations exceeding the bond dissociation energies (BDEs) of vulnerable bonds in the organic stack, promoting photochemical bond scission and the formation of non-radiative defects.[9,12,13] Critically, any device- or materials-level factor that promotes carrier accumulation (*e.g.*, trap-assisted localization) can elevate local exciton/charge densities, thereby increasing the probability of destructive annihilation events and accelerating defect generation during operation.[14]

Within this context, the host material plays an essential role, particularly for blue TADF, where the energetic constraints are most severe.[2] For blue OLEDs, the host must combine a wide electronic gap and a triplet energy (T_1) higher than the emitter to prevent Dexter-type triplet leakage, while also supporting morphological stability, balanced carrier transport to broaden the recombination zone and reduce local exciton/charge density.[2,15] Importantly, the high T_1 required for blue emission (2.8–3.0 eV) is close to the BDE scale of many common organic bonds.[11,16,17] This makes the chemical robustness of the host, including in charged (anionic and cationic) states, crucial for

[a] Institute of Photonics and Nanotechnology, Faculty of Physics, Vilnius University, Saulėtekio av. 3, LT-10257 Vilnius, Lithuania. E-mail: karolis.kazlauskas@ff.vu.lt
[b] Department of Polymer Chemistry and Technology, Faculty of Chemical Technology, Kaunas University of Technology, Baršausko 59, LT-51423, Kaunas, Lithuania

extending device lifetime. At the same time, operational stability can remain limited even for chemically robust hosts if solid-state packing and energetic disorder generate deep traps that drive carrier pile-up, compress the recombination zone, and enhance exciton–polaron interactions.[12,18] Therefore, suppressing carrier traps is a central yet often overlooked materials objective for stable blue TADF-OLEDs.

Many widely used high-triplet-energy hosts are carbazole-based (*e.g.*, with mCP-derived motifs), yet a well-documented weakness is the comparatively low dissociation energy of certain C–N bonds in the anionic state.[19–23] For some derivatives, anionic C–N cleavage can occur at BDE as low as ~1.3–2.0 eV, providing a plausible molecular origin for host-mediated degradation under electrical stress.[24–28] This motivates the search for alternative host frameworks that retain high T_1 while eliminating fragile bonds and increasing charge-state-dependent BDE. However, host design must be evaluated not only through intrinsic bond strength, but also through the solid-state charge dynamics imposed by molecular packing.

Dibenzofuran (DBF)-based host architectures featuring a rigid, fused, oxygen-bridged motif are promising in this respect, as they support high T_1 and can be incorporated into host backbones while avoiding the most labile C–N linkages.[29,30] In addition to their relevance for blue TADF,[31] DBF-containing hosts have also been explored in blue phosphorescent OLEDs. Extensive contributions from J. Y. Lee and coworkers include the development of DBF-containing high-T_1 hosts and hole/exciton-blocking materials, which enhance the performance and stability of blue devices.[30,32–35] These studies support DBF-centered architectures as compatible with the demanding energetics of blue emission and well-positioned to address lifetime limitations through enhanced resistance to charge-induced decomposition. Furthermore, DBF scaffolds also provide platforms for subtle structural variations (*e.g.*, linkage position and steric substitution)[34,36] to tune packing density, energetic disorder, and charge trapping, which can dominate efficiency roll-off and device lifetime.

Here, we investigate high-triplet-energy DBF-biphenyl host materials tailored for stable blue TADF-OLED operation, leveraging DBF linkage (2- *vs*. 4-position) and *tert*-butyl substitution as control factors to modulate solid-state charge dynamics without compromising intrinsic chemical stability. Rather than focusing on the peak device metrics, we emphasize a systematic comparative evaluation of how subtle host structural variations influence charge transport, recombination behavior, and operational stability within an otherwise identical blue TADF-OLED architecture. To this end, we combine multi-state BDE calculations and thermal analysis with neat-film photophysics, single-carrier transport measurements, and doped blue OLED studies to correlate host structure with EQE, roll-off, and operational lifetime. Crucially, we utilize impedance spectroscopy under operating bias and equivalent-circuit analysis to probe trap-limited transport and carrier accumulation, enabling a device-physics-based view of host-dependent recombination and degradation. Ultimately, we pinpoint charge trapping as the major lifetime factor within this DBF host series.

2. Experimental

2.1. Materials

Dibenzo[*b*,*d*]furan-2-ylboronic acid, dibenzo[*b*,*d*]furan-4-ylboronic acid, bis(triphenylphosphine) palladium(II) dichloride [$PdCl_2(PPh_3)_2$], and 2,2′-dibromo-4,4′-di-*tert*-butyl-1,1′-biphenyl were purchased from BLD Pharm. 2,2′-Dibromobiphenyl was purchased from Thermo Scientific. Potassium carbonate (K_2CO_3), sodium chloride (NaCl), and solvents were purchased from Eurochemicals. Unless otherwise specified, all commercially sourced materials were used as received.

Unless stated otherwise, organic materials for OLED fabrication were obtained from commercial suppliers in sublimed grade and used as received. 4,6-Bis(1-methylcarbazol-9-yl)benzene-1,3-dicarbonitrile (DMeCzIPN) was synthesized following the reported literature procedure[37] and further purified by vacuum sublimation prior to device fabrication.

2.2. Methods

The chemical structures of the synthesized compounds were confirmed by NMR spectroscopy and single-crystal X-ray diffraction (SC-XRD). ^{1}H and ^{13}C NMR spectra were recorded with a Bruker Avance III spectrometer (400 and 101 MHz, respectively) at 298 K in THF-d_8 and $CDCl_3$. Elemental analysis was conducted using the Exeter Analytical CE-400 elemental analyzer.

Single crystals for SC-XRD were obtained by slow evaporation of acetone solutions of the target compounds. **DBF4-BPh(*t*Bu)** crystals were grown from a THF/methanol mixture. Diffraction data were collected on an XtaLAB Synergy diffractometer (Rigaku) equipped with a HyPix-6000HE hybrid photon-counting detector and a PhotonJet microfocus Cu Kα source (λ = 1.54184 Å). Data were collected and processed using CrysAlisPro. The crystal structures were solved by intrinsic phasing with SHELXT[38] and refined by full-matrix least-squares minimization using SHELXL[39] through the Olex2 interface.[40] Crystallographic data have been deposited with the Cambridge Crystallographic Data Centre (CCDC 2525285, 2525286, 2525288, and 2525294).

Thermogravimetric analysis (TGA) and differential scanning calorimetry (DSC) were performed using a TA Instruments TGA Q50 and DSC Q2000, respectively. TGA measurements were conducted under a nitrogen atmosphere with a heating rate of 20 °C min^{-1}. The thermal decomposition temperature ($T_{-5\%}$) is reported as the temperature at 5% weight loss. DSC measurements were carried out under nitrogen in sealed aluminum pans at a heating rate of 10 °C min^{-1}.

Ground-state geometries were optimized in toluene using density functional theory (DFT) with the B3LYP functional and the 6-31G(d) basis set as implemented in Gaussian 09W. Excited-state energies (S_1 and T_1), oscillator strengths, and frontier orbital energies (HOMO/LUMO) were computed using the Tamm–Dancoff approximation (TDA) to TD-DFT at the same level of theory in toluene, based on the optimized ground-state geometries. Bond dissociation energies (BDEs) were calculated consistently at the same level for neutral,

cationic, and anionic states by optimizing the intact molecule and its dissociation fragments.

UV-vis absorption spectra were recorded using a Perkin-Elmer Lambda 950 UV–vis-NIR spectrophotometer. Neat films were prepared by spin-coating chloroform solutions (10 mg mL^{-1}) onto quartz substrates at 2000 rpm, followed by annealing at 50 °C for 15 min to remove residual solvent. Steady-state photoluminescence (PL) spectra were recorded using a Hamamatsu PMA-11 back-thinned CCD detector with a xenon lamp coupled to a monochromator as the excitation source (excitation wavelength, 295 nm). PL quantum yields (PL QY) of thin films were determined using an integrating sphere (SphereOptics), following the widely used de Mello integrating-sphere protocol for thin films.[41] Low-temperature measurements were conducted using a closed-cycle helium cryostat (Cryo Industries 204N). Phosphorescence spectra were measured under pulsed excitation using an Ekspla NT 242 YAG:Nd^{3+} laser (OPO output at 300 nm, 5 ns pulse width, 1 kHz repetition rate) and detected with a time-gated iStar DH340T ICCD camera (Andor) mounted on a Shamrock SR-303i spectrograph. Triplet energies were determined from the onset of the phosphorescence spectra.

Cyclic voltammetry (CV) was performed with an eDAQ 466 potentiostat in a three-electrode cell (glassy carbon working, Pt/Ti counter, Ag/AgCl reference) in N_2-purged DMF containing 0.1 M *n*-Bu_4NBF_4 at 2.0 mM analyte concentration and 100 mV s^{-1} potential scan rate. Potentials were referenced to the Fc/Fc^+ redox couple measured under identical conditions. Energy levels were converted to the vacuum scale using the commonly applied −4.99 eV offset for Fc/Fc^+.[42]

Patterned ITO/glass substrates (Kintec) employed for OLED fabrication were sequentially sonicated in Hellmanex II, deionized water, acetone, and isopropanol, then treated with O_2 plasma for 10 min. Substrates were transferred into a multichamber thermal-evaporation system (base pressure $< 1 \times 10^{-6}$ Torr) housed in a nitrogen glovebox. Organic layers were deposited at ∼1 Å s^{-1} with thicknesses and deposition rate monitored by a quartz crystal microbalance. Without breaking the vacuum, LiF and Al were deposited at 0.2 and 1 Å s^{-1}, respectively. The device active area was 2×2 mm^2, defined by the patterned ITO and cathode shadow mask. Devices were transferred to the glovebox without exposure to air and encapsulated using a glass lid and UV-curable epoxy (KATIOBOND LP655; DELO). For each host, 4–8 devices with identical EML composition (20 wt% DMeCzIPN) were fabricated and measured. The electroluminescence (EL) performance metrics and stability trends reported were reproducibly observed across devices.

EL spectra, current–voltage–luminance (*I–V–L*) characteristics, external quantum efficiency (EQE), and efficiency roll-off were measured at room temperature using a calibrated integrating-sphere system (ORB Optronix) coupled to a RadOMA GS-1290 spectroradiometer and a Keithley 2601A source meter. Device operational lifetimes were measured under constant-current-density drive using a Keysight U2722A source-measure unit, while luminance was continuously monitored with a calibrated silicon photodiode (Thorlabs). Lifetime metrics (LT_{50}) are defined as the elapsed time to 50% of the initial luminance under the specified drive conditions. Impedance spectroscopy was performed using a Keithley 4200A parameter analyzer by applying a 20 mV AC perturbation over the frequency range 1 kHz to 1 MHz.

3. Results and discussion

3.1. Synthesis and theoretical analysis

The detailed synthesis of the host materials **DBF2-BPh**, **DBF4-BPh**, **DBF2-BPh(*t*Bu)**, **DBF4-BPh(*t*Bu)** is described in SI. The materials were obtained in moderate yields and well characterized by NMR and elemental analysis (Fig. S13–S20). All hosts were purified by vacuum sublimation to obtain pure compounds for photophysical studies and device fabrication.

3.1.1. DFT calculations. DFT calculations (B3LYP/6-31G(d)) reveal that the HOMOs of all DBF–biphenyl hosts are distributed over the full backbone, evidencing substantial conjugative coupling (Fig. 1). The LUMOs are likewise distributed across the backbone. However, in the *tert*-butyl-substituted derivatives (**DBF2-BPh(*t*Bu)**, **DBF4-BPh(*t*Bu)**), the LUMO density is slightly displaced from the biphenyl core toward the DBF fragments, while the *tert*-butyl groups remain electronically inactive.

These frontier-orbital topologies are consistent with the calculated excited-state parameters (Table 1). All hosts display high S_1 (4.08–4.20 eV) and T_1 (3.05–3.15 eV) levels suitable for blue-exciton confinement. A pronounced regioisomeric linkage effect is observed: hosts bearing 2-linked DBF units (**DBF2-BPh**, **DBF2-BPh(*t*Bu)**) show higher S_1 and T_1 and ∼one order of magnitude larger oscillator strengths (f = 0.046–0.056) than the 4-linked analogues (**DBF4-BPh**, **DBF4-BPh(*t*Bu)**; f = 0.0022–0.0033). This trend is attributed to the altered conjugation pathways and electronic coupling imposed by the DBF connection site, which modulates the transition dipole and the balance between more allowed (brighter) *versus* coupling-suppressed (darker) $S_0 \rightarrow S_1$ excitations. In contrast, *tert*-butyl substitution has a negligible impact on S_1/T_1, as reflected by the near-identical energies within each linkage pair (**DBF2-BPh** *vs.* **DBF2-BPh(*t*Bu)**; **DBF4-BPh** *vs.* **DBF4-BPh(*t*Bu)**), consistent with its primarily steric/morphology-tuning role.

3.1.2. BDE calculations. The intrinsic chemical stability of the host materials was evaluated by calculating adiabatic bond dissociation energies (BDEs) for the most relevant σ-bonds in the neutral, cationic, and anionic states (Table S1 and Fig. S1). For easier comparison, the BDE data are also presented as a bar chart in Fig. S2. The analyzed bonds are those indicated in Fig. S1: B1 (central biphenyl C–C), B2 (DBF–biphenyl C–C), and B3 (*tert*-butyl–aryl C–C).

In the neutral state, all hosts exhibit high bond strengths, indicating intrinsically robust backbones (B1 ≈ 4.56–4.66 eV, B2 ≈ 4.81–4.87 eV, B3 ≈ 3.93 eV). The cationic-state BDEs likewise remain sufficiently high across the series (B1 ≈ 3.57–3.63 eV, B2 ≈ 3.14–3.89 eV, B3 ≈ 2.86–3.02 eV). Notably, the 2-linked DBF hosts retain higher B2(cation) values (3.87–3.89 eV) than the 4-linked analogues (3.14–3.16 eV), suggesting a modest lowering of the DBF–biphenyl junction strength upon 4-linkage

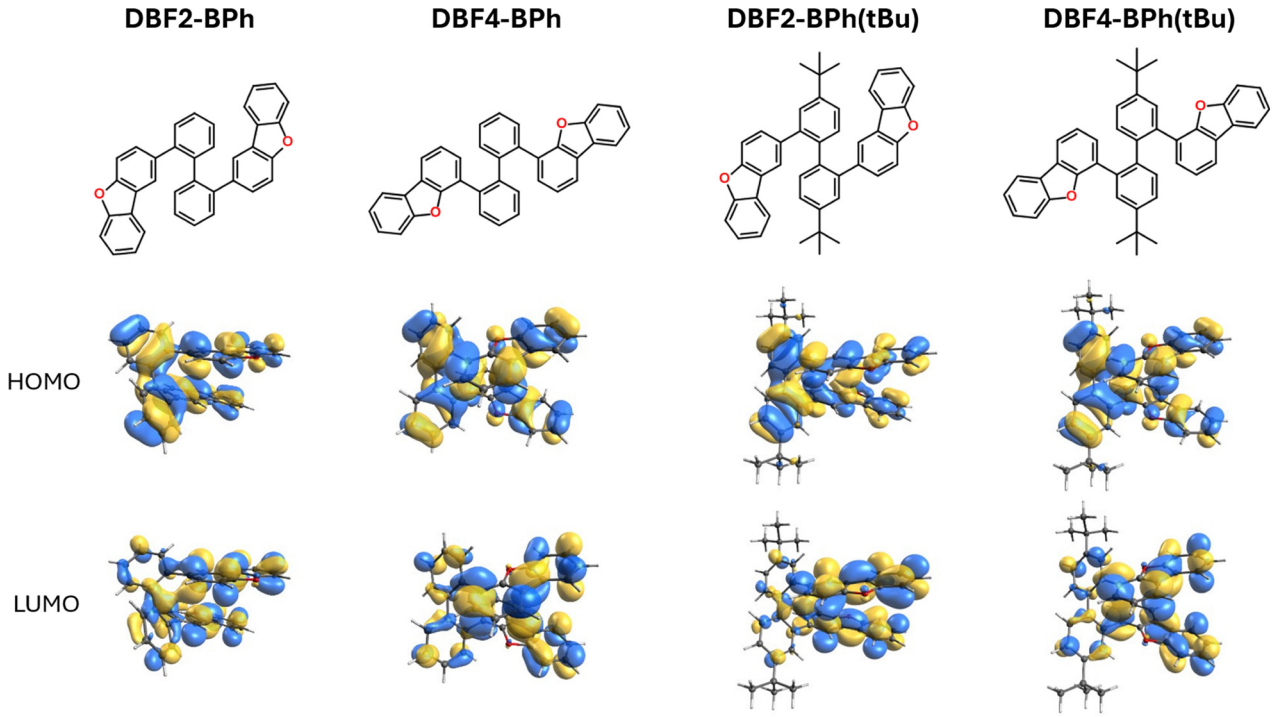

Fig. 1 Molecular structures and HOMO/LUMO distributions of the DBF-biphenyl hosts obtained by DFT B3LYP/6-31G(d) calculations.

Table 1 First singlet- and triplet-excited-states energies and oscillator strengths of the studied compounds calculated by TDA of TD-DFT (B3LYP/6-31G(d)) in toluene at optimized ground-state geometry

Compound	S_1 (eV)	f, $S_0 \rightarrow S_1$	T_1 (eV)
DBF2-BPh	4.1954	0.0460	3.1492
DBF4-BPh	4.1132	0.0022	3.0545
DBF2-BPh(*t*Bu)	4.1782	0.0564	3.1496
DBF4-BPh(*t*Bu)	4.0828	0.0033	3.0513

under hole-rich conditions. In the anionic state, although the DBF–biphenyl bond (B2) is consistently weakened across all hosts, the BDEs remain relatively high (2.38–2.44 eV). *tert*-Butyl substitution has a negligible impact on the anionic BDE (**DBF2-BPh** *vs.* **DBF2-BPh(*t*Bu)**; **DBF4-BPh** *vs.* **DBF4-BPh(*t*Bu)**), confirming its primarily steric role.

Importantly, these values compare favorably with the widely discussed anionic C–N bond fragility in carbazole/arylamine-based hosts (typically ~1.3–2.0 eV),[24–28] indicating enhanced resilience to electron-induced bond cleavage in the present DBF–biphenyl framework. The multi-state BDE analysis supports that the studied hosts are chemically robust and well-suited for OLED applications. It also suggests that the performance differences discussed below are more likely governed by electronic structure and/or morphological factors than by intrinsic bond instability.

3.2. Thermal and electrochemical properties

Thermal properties of the DBF–biphenyl hosts were evaluated by TGA and DSC (Fig. S3 and Table S2). All compounds were isolated as crystalline solids, yet upon thermal treatment, they readily formed molecular glasses, as evidenced by distinct glass transitions in the second DSC heating scan. The measured T_g values span 69–94 °C (Table S2).

The unsubstituted hosts **DBF2-BPh** and **DBF4-BPh** additionally showed crystallization signals in the repeated heating scans (T_{cr} = 137 and 155 °C, respectively) followed by melting transitions (T_m = 234 and 249 °C). By contrast, the *tert*-butyl-substituted hosts **DBF2-BPh(*t*Bu)** and **DBF4-BPh(*t*Bu)** exhibited no crystallization exotherms in the second heating scan, consistent with steric inhibition of efficient packing and improved morphological stability of the glassy state. TGA measurements confirmed high thermal robustness of the compounds, with 5% weight-loss temperatures ($T_{-5\%}$) of 293–318 °C, supporting sufficient stability for vacuum thermal processing and device operation.

The frontier orbital energy levels of the hosts were estimated by combining electrochemical reduction onsets from cyclic voltammetry (CV) with optical bandgaps (E_g) obtained from thin-film absorption (Table 2 and Fig. S4). For all hosts, the CV traces displayed a well-defined irreversible/weakly quasi-reversible reduction wave, whereas no oxidation process was detected within the accessible electrochemical window. Consequently, LUMO energies were derived directly from the onset of the reduction potentials, while HOMO energies were estimated using HOMO = LUMO − E_g and thus should be treated as approximate. Nevertheless, because all the hosts share closely related conjugated frameworks and nearly identical E_g values, we consider the relative HOMO trends across the series to be reliable.

Table 2 Photophysical and electrochemical properties of the DBF–biphenyl hosts

Material	E_g[a], eV	S_1[b], eV	T_1[c], eV	HOMO[d], eV	LUMO[e], eV
DBF2-BPh	3.91	3.89	2.81	−5.99	−2.24
DBF4-BPh	3.94	3.85	2.87	−6.13	−2.33
DBF2-BPh(*t*Bu)	3.91	3.86	2.77	−5.80	−2.05
DBF4-BPh(*t*Bu)	3.94	3.82	2.77	−6.11	−2.33

[a] Calculated from the lowest energy peak of neat film absorption spectrum. [b] Calculated from the onset of neat film RT PL spectrum. [c] Calculated from the onset of neat film Phos. spectrum. [d] HOMO = LUMO − E_g. [e] Determined from the CV reduction potential using Fc/Fc^+ = −4.99 eV *vs.* vacuum.[42]

All hosts exhibited consistently large E_g of 3.91–3.94 eV, yielding deep-lying HOMO levels and relatively shallow LUMO levels typical of wide-gap, high-triplet-energy host frameworks. The LUMO energies spanned a range from −2.05 to −2.33 eV, while the derived HOMO energies lay between −5.80 and −6.13 eV. Notably, **DBF4-BPh/DBF4-BPh(*t*Bu)** showed systematically deeper HOMO/LUMO energies than the 2-linked analogues (**DBF2-BPh/DBF2-BPh(*t*Bu)**), consistent with a modest increase in electron affinity associated with the altered DBF–biphenyl connectivity. *tert*-Butyl substitution was found to have little effect on the frontier energies.

3.3. Photophysical properties

The photophysical properties of the host materials were assessed by absorption and photoluminescence (PL) spectroscopy to elucidate their suitability for exciton confinement in OLEDs. Considering that hosts are utilized in condensed phases in emissive layers (EMLs), the properties were determined for device-relevant neat films, where intermolecular interactions can affect excited-state energies. The neat-film absorption spectra of the DBF–biphenyl hosts are dominated by intense UV π–π* transitions, and the corresponding room-temperature PL spectra show broad near-UV emission typical of rigid, wide-gap aromatic frameworks (Fig. 2a). The optical bandgaps extracted from the lowest-energy absorption features are similar across the series (E_g = 3.91–3.94 eV, Table 2), indicating insensitivity of the *tert*-butyl substitution or the DBF linking pattern to the overall gap. Consistent with the DFT results, the 2-linked hosts (**DBF2-BPh/DBF2-BPh(*t*Bu)**) exhibited slightly higher singlet energies (S_1 = 3.86–3.89 eV) than the 4-linked analogues (**DBF4-BPh/DBF4-BPh(*t*Bu)**; S_1 = 3.82–3.85 eV), reflecting linkage-dependent modulation of the effective conjugation pathway and transition character.

Triplet energies were determined from time-gated low-temperature phosphorescence of neat films (Fig. 2b), yielding T_1 = 2.77–2.87 eV (Table 2). **DBF4-BPh** expressed the highest T_1 of 2.87 eV, followed by **DBF2-BPh** (2.81 eV), while the *tert*-butyl derivatives **DBF2-BPh(*t*Bu)/DBF4-BPh(*t*Bu)** exhibited slightly lower values (2.77 eV). Thus, the neat-film T_1 energies are comparable to those of the commonly used carbazole–biphenyl benchmark mCBP ($T_1 \approx$ 2.80–2.85 eV),[43,44] supporting the suitability of the DBF–biphenyl hosts for triplet confinement in typical blue/sky-blue TADF devices.

3.4. Charge transport and operational stability in blue OLEDs

Hole-only (HOD) and electron-only (EOD) devices were fabricated to probe majority-carrier transport through the host layers. In HODs (Fig. 3a), the host layer was sandwiched between Tris-PCz layers to ensure hole-dominated conduction, whereas the high-lying LUMO of Tris-PCz and the absence of LiF suppressed electron injection. In EODs (Fig. 3b), the deep HOMO of T2T blocked holes while the BPy-TP2/LiF/Al cathode facilitated electron injection. No electroluminescence was observed from either HODs or EODs, consistent with predominantly single-carrier transport through the host layer.

The *I–V* plots revealed two distinct structure–property relationships (Fig. 3c). *tert*-Butyl substituted **DBF2-BPh(*t*Bu)** and **DBF4-BPh(*t*Bu)** exhibited dramatically enhanced electron currents relative to the unsubstituted **DBF2-BPh** and **DBF4-BPh**. At 6 V, the electron current densities increased by 3–4 orders of magnitude from (2–5) × 10^{-4} mA cm^{-2} (**DBF2-BPh/DBF4-BPh**) to ∼0.9–1.5 mA cm^{-2} (**DBF4-BPh(*t*Bu)/DBF2-BPh(*t*Bu)**). This enhancement could not be explained solely by frontier-level

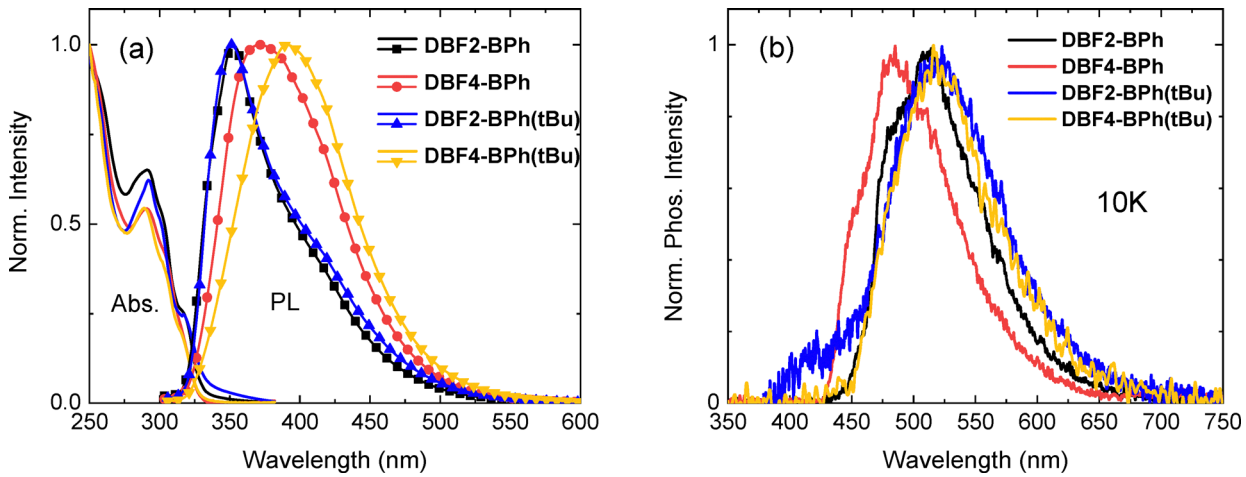

Fig. 2 (a) Absorption (solid lines) and room-temperature PL (lines + symbols) spectra of neat films of the DBF-biphenyl hosts. (b) Low-temperature phosphorescence spectra of neat films recorded at 10 K with a 3 ms delay.

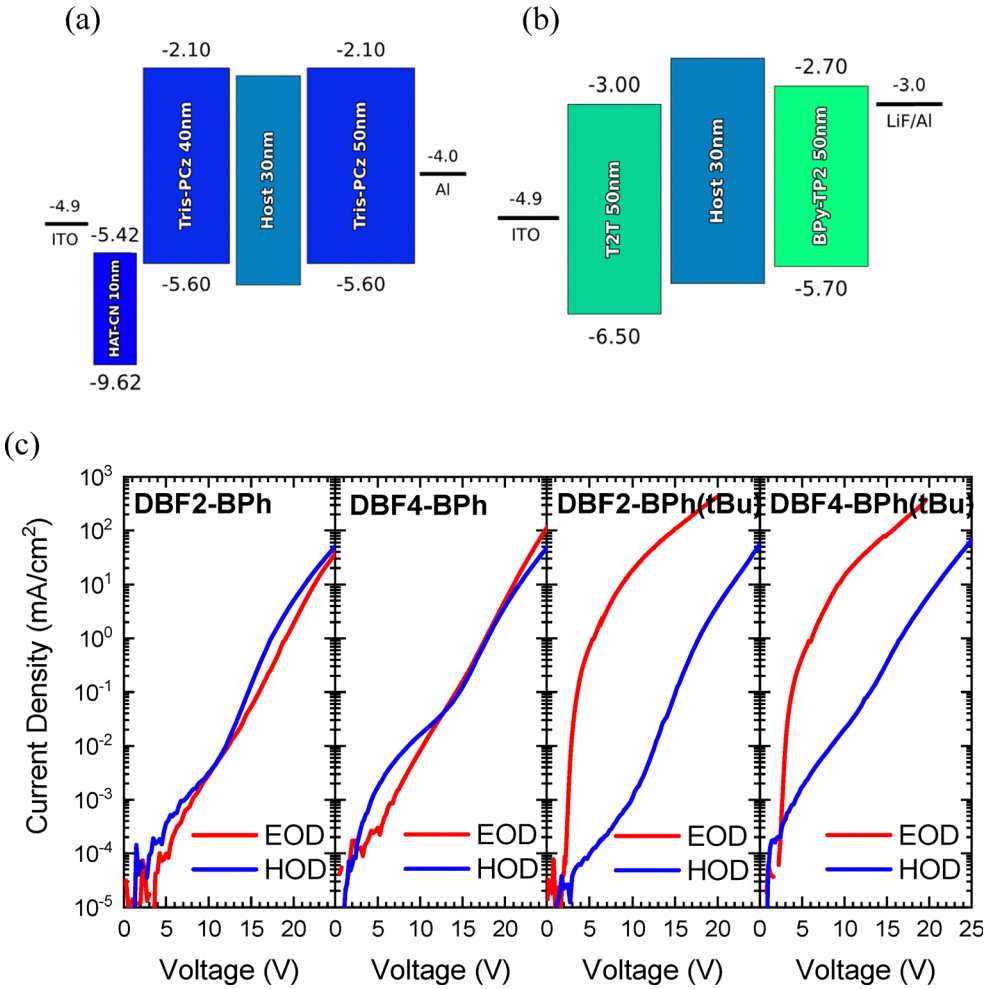

Fig. 3 Energy level alignment and single-carrier characteristics of the DBF–biphenyl hosts. (a) Energy diagram of HOD and (b) EOD architectures. (c) *I–V* curves of neat film HODs (blue) and EODs (red) based on different hosts (indicated). Energy levels are referenced to vacuum and given in eV.

alignment. Notably, **DBF2-BPh(*t*Bu)** has the shallowest LUMO (the largest electron-injection barrier) yet the highest electron current, indicating that bulk transport factors, such as morphology and energetic disorder, dominate electron conduction. In this context, the suppressed crystallization of the *tert*-butyl hosts, as evidenced by DSC, indicates improved morphological stability of the amorphous glassy phase and suggests a modified molecular packing landscape that can facilitate electron percolation in neat films. On the other hand, hole transport varied more moderately and correlated primarily with the DBF–biphenyl connection site. At 6 V, 4-linked hosts **DBF4-BPh** and **DBF4-BPh(*t*Bu)** showed hole current densities of $\sim 3 \times 10^{-3}$ mA cm^{-2}, roughly an order of magnitude higher than their 2-linked counterparts **DBF2-BPh** (5.6×10^{-4} mA cm^{-2}) and **DBF2-BPh(*t*Bu)** (1.5×10^{-4} mA cm^{-2}). Thus, in neat films, **DBF2-BPh** and **DBF4-BPh** displayed more balanced (ambipolar) transport, whereas **DBF2-BPh(*t*Bu)** and **DBF4-BPh(*t*Bu)** were electron-dominant.

Interestingly, the pronounced differences in the electron transport between the *tert*-butyl–substituted and unsubstituted hosts disappeared upon doping with DMeCzIPN emitter at 20 wt% (Fig. 4), which reflects the OLED emissive layer composition. DMeCzIPN, a previously reported efficient blue TADF emitter with a triplet energy of 2.79 eV, was employed as the dopant.[37] This loading was selected because 20 wt% DMeCzIPN corresponds to a near-saturated PL QY of the EML (Fig. S5). The convergence of the *I–V* characteristics in the emitter-doped films (Fig. 4) indicates that charge conduction becomes largely dopant-mediated, rather than being dictated by the intrinsic electron current of the neat host alone. Accordingly, neat-film transport trends are best interpreted as indicators of intrinsic host conduction, whereas stability-relevant carrier accumulation and trapping must be assessed under operating bias in complete devices (see Section 3.5).

To enable a direct comparison of host effects on electroluminescence (EL) and stability, the blue TADF-OLEDs were fabricated with an identical multilayer stack: ITO/HAT-CN (10 nm)/Tris-PCz (30 nm)/mCBP (10 nm)/EML (30 nm)/T2T (10 nm)/BPy-TP2 (40 nm)/LiF (0.8 nm)/Al (100 nm) (Fig. 5a). The molecular structures of all materials employed are provided in Fig. S6. In this configuration, ITO serves as the transparent anode, while HAT-CN (1,4,5,8,9,11-hexaazatriphenylenehexacarbonitrile) acts as an efficient hole-injection interlayer. Tris-PCz

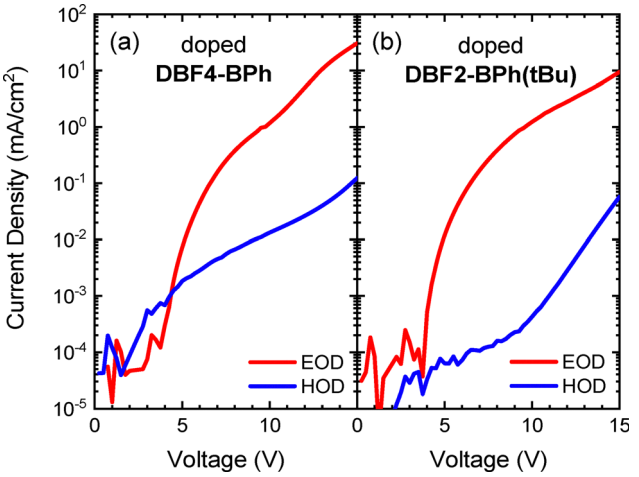

Fig. 4 Representative *I*–*V* curves of HODs (blue) and EODs (red) based on (a) **DBF4-BPh** and (b) **DBF2-BPh(*t*Bu)** hosts doped with 20 wt% of DMeCzIPN emitter.

(9-phenyl-3,6-bis(9-phenyl-9H-carbazol-3-yl)-9H-carbazole) provides efficient hole transport and suppresses electron leakage toward the anode side. A thin mCBP (3,3′-di(9H-carbazol-9-yl)-1,1′-biphenyl) layer is inserted as an additional hole-transporting and exciton-blocking spacer to help confine recombination within the EML. The EML is the only variable across devices and consists of each DBF-biphenyl host doped with 20 wt% DMeCzIPN. On the cathode side, T2T (2,4,6-tris(biphenyl-3-yl)-1,3,5-triazine) functions primarily as a hole-blocking layer to retain carriers and excitons in the EML. Finally, BPy-TP2 (2,7-di(2,2′-bipyridin-5-yl)triphenylene) serves as the electron-transport layer, while LiF/Al forms the cathode, with LiF enhancing electron injection into the BPy-TP2. For each host, 4–8 devices with identical EML compositions were fabricated and measured. The resulting EL performance and stability trends discussed below were consistently reproduced. Device-to-device reproducibility data are provided in Fig. S8–S11. We note that the aim here is not merely to identify the host delivering the best performance, but to determine, through a controlled comparative series, which host-dependent factors govern device stability under practical operating conditions.

The EL performance of blue TADF-OLEDs using the four DBF-biphenyl hosts is summarized in Fig. 5, Fig. S7 and Table 3. All devices turn on at the same voltage (V_{on} = 3.25 V),

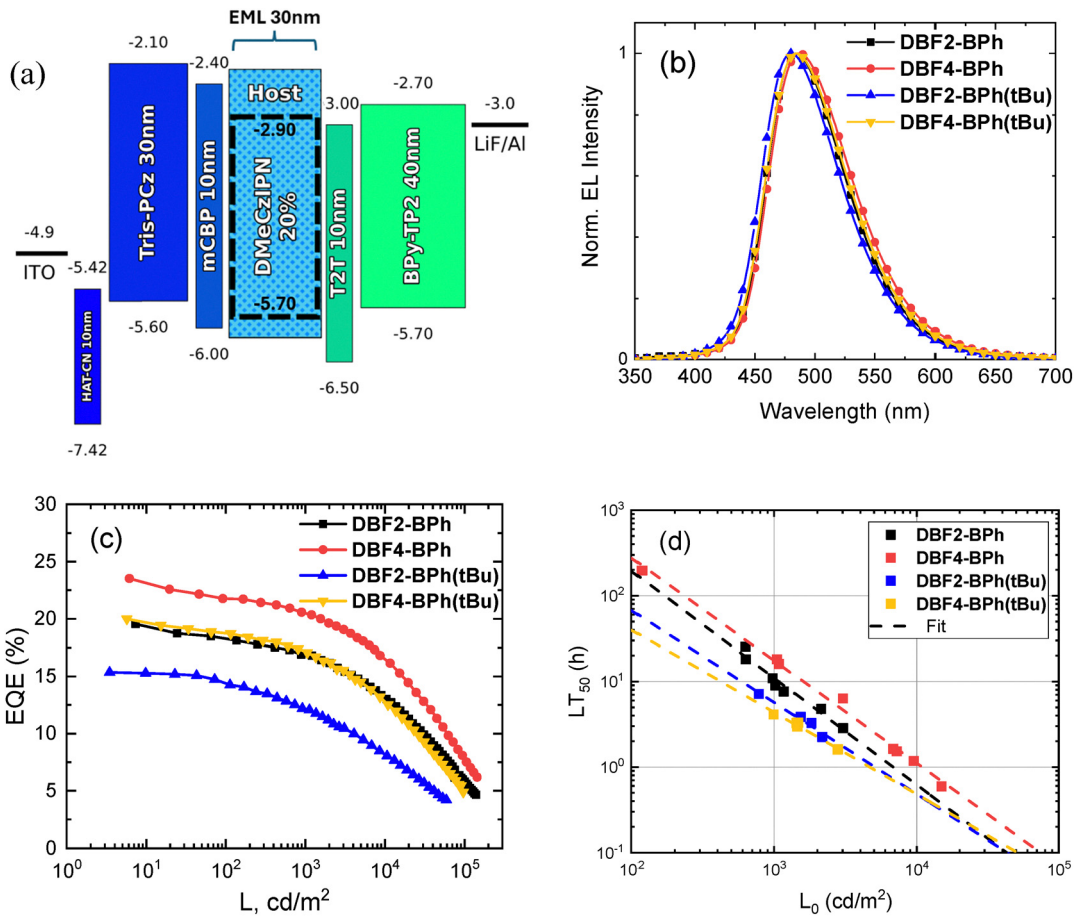

Fig. 5 Device structure and performance of blue TADF-OLEDs based on the DBF-biphenyl hosts doped with 20 wt% DMeCzIPN: (a) energy level diagram referenced to vacuum (eV), (b) EL spectra at 10 mA cm^{-2}, (c) EQE as a function of luminance, and (d) operational half-lifetime (LT_{50}) at different initial luminance (L_0) with fits (dashed lines). Each point corresponds to a distinct device measured (Fig. S8–S11).

Table 3 Main EL parameters of DMeCzIPN-based blue TADF-OLEDs using **DBF2-BPh**, **DBF4-BPh**, **DBF2-BPh(*t*Bu)**, and **DBF4-BPh(*t*Bu)** as hosts

Host	V_{on}, V	$V_{@1000\ cd\ m^{-2}}$, V	EQE[a], %	LT_{50}[b], h	λ_{max}, nm	CIE, (x, y)
DBF2-BPh	3.25	5	19.5/18.1/16.8	193/10.9	485	(0.18, 0.35)
DBF4-BPh	3.25	5.5	23.5/22/20.5	275/17.5	488	(0.19, 0.38)
DBF2-BPh(*t*Bu)	3.25	6.5	15.6/14.3/12.1	51.9/6.5	483	(0.17, 0.33)
DBF4-BPh(*t*Bu)	3.25	6	20/18.7/17.1	38.6/4.4	486	(0.18, 0.36)

[a] EQE_{max}/@100 cd m^{-2}/@1000 cd m^{-2}. [b] @100 cd m^{-2}/@1000 cd m^{-2}.

indicating comparable charge injection thresholds. The observed performance differences, therefore, mainly reflect host-dependent charge balance and loss pathways within the EML. The EL spectra are very similar for all hosts, with only a small shift of the EL maximum (λ_{max} = 483–488 nm), indicating that emission is dominated by the DMeCzIPN emitter[37] rather than host-derived or exciplex emission (Fig. 5b). This small shift is most likely a minor host-matrix effect, potentially reflecting reduced intermolecular interactions between DMeCzIPN molecules in the bulkier *tert*-butyl-substituted hosts. The operating voltages at 1000 cd m^{-2} fall within a range of 5.0–6.5 V (Table 3 and Fig. S7b), with *tert*-butyl-substituted hosts requiring higher values, consistent with more resistive transport and/or increased trap involvement, as discussed in Section 3.5. In terms of efficiency, **DBF4-BPh** delivers the best device metrics with EQE_{max} = 23.5% and only modest roll-off to 22.0% at 100 cd m^{-2} and 20.5% at 1000 cd m^{-2} (Fig. 5c and Table 3). **DBF2-BPh** shows a slightly lower EQE_{max} of 19.5% but a similar roll-off trend. The superior efficiencies of the 4-linked hosts, most evident for **DBF4-BPh**, are consistent with the linkage-enhanced hole transport observed in single-carrier devices. This structure-transport relationship has also been noted for biphenyl-based host series in the blue TADF literature, where linking pattern controls charge balance and recombination zone position.[45] In particular, although **DBF2-BPh(*t*Bu)** and **DBF4-BPh(*t*Bu)** exhibit comparable PL QY at the device-relevant 20 wt% doping level, the lower EQE of **DBF2-BPh(*t*Bu)** is more likely attributed to less favorable charge balance, since it shows markedly poorer hole transport while remaining strongly electron-dominant. In contrast, the *tert*-butyl–substituted hosts **DBF2-BPh(*t*Bu)** and **DBF4-BPh(*t*Bu)** exhibit noticeably lower efficiencies than their unsubstituted counterparts, despite similar or slightly higher operating voltages. These trends follow the EML photophysics at 20 wt% DMeCzIPN doping, which corresponds to near-saturated film PL QY (Fig. S5). Thus, the lower PL QY of the *tert*-butyl-substituted hosts still contributes to their overall lower EQEs relative to the unsubstituted hosts. However, within the *tert*-butyl host pair, the EQE difference is more consistently explained by differences in charge balance and recombination efficiency. Such carrier imbalance can shift and possibly narrow the recombination zone, thereby increasing susceptibility to polaron-related non-radiative losses and lowering the EQE. Notably, while the EL spectra confirm that the emissive state is DMeCzIPN across all devices, the *tert*-butyl hosts exhibit near-resonant T_1 alignment, which can increase sensitivity to nonradiative losses under electrical stress, even without changing the emitting species.

Operational stability of the devices measured under a constant-current driving regime further differentiates the hosts (Fig. 5d and Table 3). At practical brightness of 1000 cd m^{-2}, **DBF4-BPh** achieves the longest lifetime (LT_{50} = 17.5 h), followed by **DBF2-BPh** (10.9 h), whereas the *tert*-butyl hosts infer significantly faster degradation (**DBF2-BPh(*t*Bu)**, 6.5 h and **DBF4-BPh(*t*Bu)**, 4.4 h). The same stability order is maintained at 100 cd m^{-2}. Given that the multi-state BDEs are comparably high across the series, the reduced lifetime in the *tert*-butyl hosts is more consistent with host-dependent solid-state disorder and trap-assisted carrier accumulation (discussed in Section 3.5), which increase exciton-polaron interactions and accelerate degradation under electrical stress.

Because the *tert*-butyl hosts exhibit a near-resonant T_1 relative to DMeCzIPN, a contribution from reduced triplet confinement (*e.g.*, partial back-transfer or enhanced nonradiative loss) cannot be fully excluded on energetic grounds alone. Yet, the identical EL spectra indicate that the emitting species remains DMeCzIPN throughout devices. Nonetheless, the magnitude and systematic nature of the lifetime differences across the series are captured most directly by the impedance response under bias (see Section 3.5), which indicates a substantially stronger trap-limited component and carrier accumulation for the *tert*-butyl hosts, consistent with accelerated exciton–polaron-mediated degradation.

3.5. Impedance spectroscopy: trap-limited transport and carrier accumulation

Small-signal impedance spectroscopy was performed to rationalize host-dependent efficiency and lifetime trends by probing trap-limited transport and carrier accumulation under operating conditions. Applied to OLED stacks, this approach enables the separation of resistive and capacitive contributions in the AC response, allowing comparative assessment of trapping-related parameters through equivalent-circuit analysis.[46,47] Importantly, the technique addresses stability-limiting carrier accumulation directly under operating bias,[48,49] offering a mechanism-level distinction of the hosts even when energetic triplet offsets are small. Measurements were collected at 6 V and 7 V to address the operating regime near 1000 cd m^{-2} and to probe how trapping/accumulation evolves with injection level. In the Nyquist (Cole–Cole) representation, the complex impedance is plotted as Im(Z) *versus* Re(Z), where each point corresponds to a different AC frequency, and the high- and low-frequency limits approach the left and right intercepts, respectively. The spectra of all devices exhibit a single dominant semicircle (Fig. 6), indicating one prevailing relaxation process

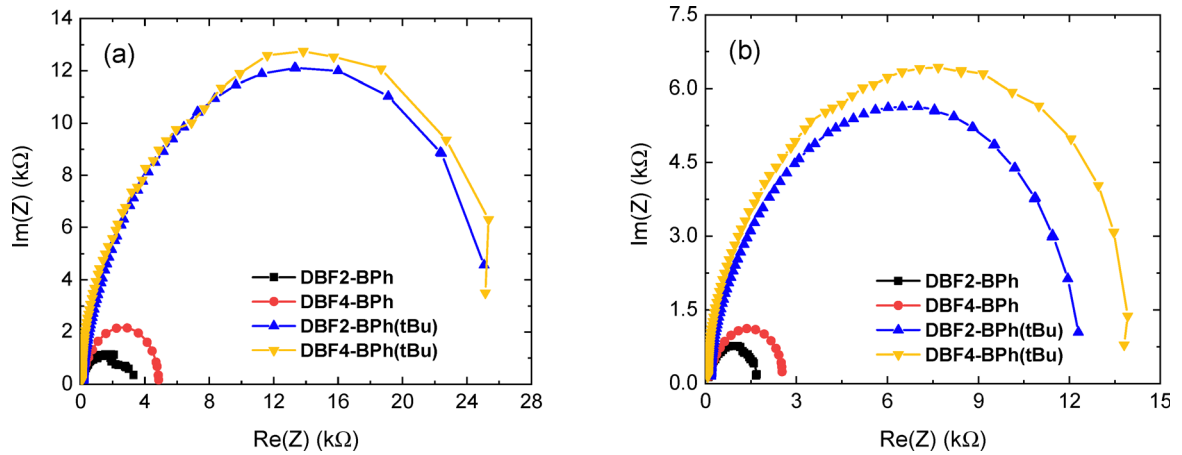

Fig. 6 Nyquist (Cole–Cole) plots of TADF-OLEDs based on the DBF-biphenyl hosts, measured under DC biases of (a) 6 V and (b) 7 V.

within the measured frequency range.[47] The impedance response is well captured by a compact $R_s + (R_p \| C_p)$ element, whereas alternative fits using a constant phase element (CPE) yield dispersion exponents $\alpha \approx 0.89$–0.98, indicating only a weak deviation from ideal capacitive behavior and supporting the simplified model for host-to-host comparison (Fig. S12 and Table S3).[47]

Across all devices, C_p is weakly bias-dependent and falls in the 0.99–1.24 nF range (Table 4), consistent with a capacitance dominated by device geometry rather than strong low-frequency charge storage in the measured window. Using the parallel-plate capacitor model, $C = \varepsilon_0 \varepsilon_r A/d$, with typical relative permittivity for organic layers $\varepsilon_r \approx 3.5$,[50] gives $C \approx 0.95$ nF for the device area $A = 4$ mm^2 and the total thickness of the organic layers $d \approx 130$ nm, matching the observed C_p magnitude. The extracted series resistance R_s values remain in the same order across hosts and both biases ($\sim$80–190 Ω), consistent with dominant contributions from contacts and transport layers common to all devices.[46]

In contrast, the parallel resistance R_p shows a strong host dependence. The *tert*-butyl-substituted hosts exhibit R_p substantially larger than the unsubstituted analogues at both biases (Table 4). At 6 V, R_p increases from 2.5–4.5 kΩ for **DBF2-BPh** and **DBF4-BPh** to 22–23 kΩ for **DBF2-BPh(*t*Bu)** and **DBF4-BPh(*t*Bu)**. At 7 V, R_p decreases for all devices as injection increases and traps are progressively filled,[48] yet **DBF2-BPh(*t*Bu)** and **DBF4-BPh(*t*Bu)** still retain 11.6–13.1 kΩ compared with 1.5–2.3 kΩ for **DBF2-BPh** and **DBF4-BPh**. Within this compact circuit, R_p is an effective resistance associated with the dominant relaxation process in the measured frequency window and should not be interpreted as a direct mobility. Accordingly, in the present work, R_p is used only as a comparative parameter of trapping-related resistive relaxation under bias, rather than as a direct quantitative measure of trap density or trap-energy distribution. Nevertheless, for identical device architectures with the only variable being the host material, the systematically higher R_p of the *tert*-butyl hosts indicates a larger resistive relaxation component, consistent with enhanced trapping-related transport limitation and/or altered recombination dynamics under bias.[47,49]

These impedance trends provide a consistent electrical origin for the performance differences. **DBF2-BPh** and **DBF4-BPh** exhibit lower R_p and correspondingly higher EQE and longer device lifetime, whereas **DBF2-BPh(*t*Bu)** and **DBF4-BPh(*t*Bu)** show strongly elevated R_p and 2–4-fold shorter LT_{50}. A plausible structural basis is that bulky *tert*-butyl groups reduce molecular packing efficiency and increase energetic disorder in the EML, thereby increasing the probability of carrier trapping. Under steady operation, trapped and accumulated polarons raise the likelihood of exciton-polaron interactions, which are known to promote efficiency roll-off and accelerate degradation in TADF-OLEDs.[48]

Table 4 Impedance spectroscopy parameters extracted from equivalent-circuit $R_s + (R_p \| C_p)$ fitting of DMeCzIPN-based OLEDs using the DBF-biphenyl hosts at typical operating biases

Bias voltage, V	Host	R_s, Ω	R_p, Ω	C_p, nF
6	**DBF2-BPh**	108.5	2463	1.24
	DBF4-BPh	162.6	4549	1.09
	DBF2-BPh(*t*Bu)	186.8	22 620	1.01
	DBF4-BPh(*t*Bu)	78.94	23 470	0.99
7	**DBF2-BPh**	102.1	1549	1.19
	DBF4-BPh	161.6	2322	1.08
	DBF2-BPh(*t*Bu)	187.1	11 560	0.99
	DBF4-BPh(*t*Bu)	81.43	13 090	1.00

Conclusion

Four high-triplet-energy dibenzo[*b*,*d*]furan–biphenyl (DBF–BPh) hosts were designed to reveal how DBF connectivity (2- *vs.* 4-linkage) and *tert*-butyl substitution of biphenyl govern host solid-state charge dynamics and, ultimately, blue TADF-OLED stability. The host framework is chemically robust, as supported by multi-state BDEs, with the lowest anionic-state value $\sim$2.4 eV well exceeding the fragility window often associated with anionic C–N cleavage in carbazole- and arylamine-based hosts. All the synthesized hosts exhibit high thermal stability ($T_{-5\%}$ = 293–318 °C) and form molecular glasses. Neat-film photophysics establishes high triplet energies (T_1 = 2.77–2.87 eV),

comparable to those of benchmark mCBP, supporting blue/sky-blue TADF device architectures.

Device performance and operational lifetime track systematic differences in host-dependent charge transport and accumulation behavior across the series. In DMeCzIPN-based blue OLEDs, the 4-linked hosts deliver the best balance of efficiency and stability, reaching EQE_{max} = 23.5% with low roll-off and LT_{50} = 17.5 h at 1000 cd m^{-2} (275 h at 100 cd m^{-2}). Conversely, *tert*-butyl-substituted hosts show 2–4× shorter LT_{50} values and lower EQEs despite similar energetics, BDEs, and improved glass-forming properties. Bias-dependent impedance spectroscopy identifies markedly higher parallel resistance for the *tert*-butyl hosts, consistent with enhanced trap-mediated carrier accumulation during operation. Such charge build-up is expected to amplify exciton–polaron-driven losses, accelerating degradation. Trap suppression, therefore, emerges as a key host design criterion for improving the stability of blue TADF-OLEDs.

Conflicts of interest

The authors declare no conflict of interest.

Data availability

The data that support the findings of this study are available in the supplementary information (SI) of this article. Supplementary information: synthesis, BDE and thermal analysis, electrochemical and photophysical data, impedance spectroscopy results, elemental analysis, NMR. See DOI: https://doi.org/10.1039/d6tc00748a.

CCDC 2525285, 2525286, 2525288 and 2525294 contain the supplementary crystallographic data for this paper.[51a–d]

Acknowledgements

The research was funded by a grant (No. S-MIP-21-12) from the Research Council of Lithuania (LMTLT). E.S. acknowledges funding from the Research Council of Lithuania (LMTLT), agreement No. S-PD-24-73.

References

1 H. Uoyama, K. Goushi, K. Shizu, H. Nomura and C. Adachi, *Nature*, 2012, **492**, 234–238.
2 M. Y. Wong and E. Zysman-Colman, *Adv. Mater.*, 2017, **29**, 1605444.
3 J. M. Dos Santos, D. Hall, B. Basumatary, M. Bryden, D. Chen, P. Choudhary, T. Comerford, E. Crovini, A. Danos, J. De, S. Diesing, M. Fatahi, M. Griffin, A. K. Gupta, H. Hafeez, L. Hämmerling, E. Hanover, J. Haug, T. Heil, D. Karthik, S. Kumar, O. Lee, H. Li, F. Lucas, C. F. R. Mackenzie, A. Mariko, T. Matulaitis, F. Millward, Y. Olivier, Q. Qi, I. D. W. Samuel, N. Sharma, C. Si, L. Spierling, P. Sudhakar, D. Sun, E. Tankelevičiūtė, M. Duarte Tonet, J. Wang, T. Wang, S. Wu, Y. Xu, L. Zhang and E. Zysman-Colman, *Chem. Rev.*, 2024, **124**, 13736–14110.
4 S. O. Jeon, K. H. Lee, J. S. Kim, S.-G. Ihn, Y. S. Chung, J. W. Kim, H. Lee, S. Kim, H. Choi and J. Y. Lee, *Nat. Photonics*, 2021, **15**, 208–215.
5 C.-Y. Chan, M. Tanaka, Y.-T. Lee, Y.-W. Wong, H. Nakanotani, T. Hatakeyama and C. Adachi, *Nat. Photonics*, 2021, **15**, 203–207.
6 K. R. Naveen, P. Palanisamy, M. Y. Chae and J. H. Kwon, *Chem. Commun.*, 2023, **59**, 3685–3702.
7 Z. Liu, T. Guo, J. Fang, B. Z. Tang and Z. Zhao, *J. Mater. Chem. C*, 2025, **13**, 15144–15150.
8 T. D. Raju, M. Tirupati, N. Kim, S. Muruganantham, P. K. Odugu, A. V. Kesavan, J. H. Kwon and T. G. Kim, *Mater. Horiz.*, 2026, DOI: 10.1039/D5MH02390D.
9 E. Tankelevičiūtė, I. D. W. Samuel and E. Zysman-Colman, *J. Phys. Chem. Lett.*, 2024, **15**, 1034–1047.
10 H. Noda, H. Nakanotani and C. Adachi, *Sci. Adv.*, 2018, **4**, eaao6910.
11 J. Sohn, D. Ko, H. Lee, J. Han, S.-D. Lee and C. Lee, *Org. Electron.*, 2019, **70**, 286–291.
12 S. Scholz, D. Kondakov, B. Lüssem and K. Leo, *Chem. Rev.*, 2015, **115**, 8449–8503.
13 A. S. D. Sandanayaka, T. Matsushima and C. Adachi, *J. Phys. Chem. C*, 2015, **119**, 23845–23851.
14 E. Stanzani, S. Sem, S. Züfle, B. Ruhstaller and S. Jenatsch, *Org. Electron.*, 2025, **139**, 107204.
15 M. Godumala, S. Choi, M. J. Cho and D. H. Choi, *J. Mater. Chem. C*, 2016, **4**, 11355–11381.
16 J. Jiang and J. Y. Lee, *Mater. Today*, 2023, **68**, 204–233.
17 S.-G. Ihn, D. Jeong, E. S. Kwon, S. Kim, Y. S. Chung, M. Sim, J. Chwae, Y. Koishikawa, S. O. Jeon, J. S. Kim, J. Kim, S. Nam, I. Kim, S. Park, D. S. Kim, H. Choi and S. Kim, *Adv. Sci.*, 2022, **9**, 2102141.
18 R. Coehoorn and S. van Mensfoort, *Phys. Rev. B:Condens. Matter Mater. Phys.*, 2009, **80**, 085302.
19 M. Hong, M. K. Ravva, P. Winget and J.-L. Brédas, *Chem. Mater.*, 2016, **28**, 5791–5798.
20 Q.-Y. Meng, R. Wang, H.-Y. Shao, Y.-L. Wang, X.-L. Wen, C.-Y. Yao and J. Qiao, *J. Phys. Chem. Lett.*, 2024, **15**, 4422–4429.
21 R. Wang, Q.-Y. Meng, Y.-L. Wang and J. Qiao, *CCS Chem.*, 2022, **4**, 331–343.
22 T. H. Ha, S. W. Kang, J. Y. Yoo and C. W. Lee, *Synth. Met.*, 2024, **303**, 117551.
23 D. Berenis, G. Puidokas, K. Bagdonas, G. Grybauskaitė, D. Banevičius, G. Kreiza, E. Skuodis, R. Butkutė, J. V. Gražulevičius and K. Kazlauskas, *J. Mater. Chem. C*, 2026, **14**, 5005–5016.
24 S.-B. Ko, S. Kang and T. Kim, *Chem. – Eur. J.*, 2020, **26**, 7767–7773.
25 D. H. Ahn, J. H. Maeng, H. Lee, H. Yoo, R. Lampande, J. Y. Lee and J. H. Kwon, *Adv. Optical Mater.*, 2020, **8**, 2000102.
26 Z. Wang, M. Li, L. Gan, X. Cai, B. Li, D. Chen and S.-J. Su, *Adv. Sci.*, 2019, **6**, 1802246.

27 C. Y. Yang, S. Kang, H. Jeong, H. J. Jang, Y. Lee and J. Y. Lee, *J. Mater. Chem. C*, 2020, **8**, 1697–1703.
28 T. H. Ha, S. W. Kang and C. W. Lee, *Org. Electron.*, 2024, **124**, 106960.
29 P. A. Vecchi, A. B. Padmaperuma, H. Qiao, L. S. Sapochak and P. E. Burrows, *Org. Lett.*, 2006, **8**, 4211–4214.
30 S. H. Jeong and J. Y. Lee, *Org. Electron.*, 2012, **13**, 1141–1145.
31 S. M. Cho, K. M. Youn, H. I. Yang, S. H. Lee, K. R. Naveen, D. Karthik, H. Jeong and J. H. Kwon, *Org. Electron.*, 2022, **105**, 106501.
32 S. H. Jeong and J. Y. Lee, *Org. Electron.*, 2012, **13**, 2589–2593.
33 J. G. Yu, S. Y. Byeon, S. H. Han and J. Y. Lee, *Chem. – Eur. J.*, 2017, **23**, 16044–16050.
34 K. H. Choi, J. M. Kim, W. J. Chung and J. Y. Lee, *Molecules*, 2021, **26**, 2804.
35 S. Y. Byeon, K. H. Lee and J. Y. Lee, *J. Mater. Chem. C*, 2020, **8**, 5832–5838.
36 Y. Im and J. Y. Lee, *Dyes Pigm.*, 2016, **128**, 84–88.
37 G. Kreiza, D. Berenis, D. Banevičius, S. Juršėnas, T. Javorskis, E. Orentas and K. Kazlauskas, *Chem. Eng. J.*, 2021, **412**, 128574.
38 G. M. Sheldrick, *Acta Crystallogr., Sect. A:Found. Adv.*, 2015, **71**, 3–8.
39 G. M. Sheldrick, *Acta Crystallogr., Sect. C:Found. Adv.*, 2015, **71**, 3–8.
40 O. V. Dolomanov, L. J. Bourhis, R. J. Gildea, J. A. K. Howard and H. Puschmann, *J. Appl. Cryst.*, 2009, **42**, 339–341.
41 J. C. de Mello, H. F. Wittmann and R. H. Friend, *Adv. Mater.*, 1997, **9**, 230–232.
42 G. P. Kissling, B. Ruhstaller and K. P. Pernstich, *Org. Electron.*, 2023, **122**, 106888.
43 S. A. Bagnich, A. Rudnick, P. Schroegel, P. Strohriegl and A. Köhler, *Philos. Trans. R. Soc., A*, 2015, **373**, 20140446.
44 Q. Xia, Y. Xiang, Y. Gong, S. Li, Y. Wu, Z. Wang and H. Fu, *J. Mater. Chem. C*, 2023, **11**, 6354–6359.
45 C. Y. Yang, K. H. Lee and J. Y. Lee, *Chem. – Eur. J.*, 2020, **26**, 2429–2435.
46 A. Raji, J. Park, J. Lee and J.-H. Lee, *J. Mater. Chem. C*, 2025, **13**, 19512–19534.
47 E. von Hauff, *J. Phys. Chem. C*, 2019, **123**, 11329–11346.
48 T. N. Le, E. Y. Park, V. Thangaraji and M. C. Suh, *Org. Electron.*, 2021, **99**, 106346.
49 S. Wang, J. Zhang, O. Gharbi, V. Vivier, M. Gao and M. E. Orazem, *Nat. Rev. Methods Primers*, 2021, **1**, 41.
50 X. de Vries and R. Coehoorn, *Phys. Rev. Mater.*, 2020, **4**, 085602.
51 (*a*) CCDC 2525285: Experimental Crystal Structure Determination, 2026, DOI: 10.5517/ccdc.csd.cc2qrrt2; (*b*) CCDC 2525286: Experimental Crystal Structure Determination, 2026, DOI: 10.5517/ccdc.csd.cc2qrrv3; (*c*) CCDC 2525288: Experimental Crystal Structure Determination, 2026, DOI: 10.5517/ccdc.csd.cc2qrrx5; (*d*) CCDC 2525294: Experimental Crystal Structure Determination, 2026, DOI: 10.5517/ccdc.csd.cc2qrs3d.